



## Rational design of MoS<sub>2</sub>@COF hybrid composites promoting C-C coupling for photocatalytic CO<sub>2</sub> reduction to ethane

Xianheng Yang<sup>1</sup>, Xingwang Lan<sup>1,\*</sup>, Yize Zhang, Hangshuai Li, Guoyi Bai<sup>\*</sup>

Key Laboratory of Chemical Biology of Hebei Province, College of Chemistry and Environmental Science, Hebei University, Baoding, Hebei 071002, PR China



### ARTICLE INFO

**Keywords:**

COF  
MoS<sub>2</sub>  
Interfacial charge transfer  
Photocatalytic CO<sub>2</sub> reduction  
Ethane

### ABSTRACT

Photocatalytic CO<sub>2</sub> reduction into high-value C<sub>2+</sub> products such as ethane is quite exciting but challenging due to multielectron steps involved and sluggish C-C coupling kinetics. Herein, a well-designed MoS<sub>2</sub>@COF hybrid composite is prepared for efficient and selective CO<sub>2</sub> photoreduction to C<sub>2</sub>H<sub>6</sub>. In-depth experimental and theoretical studies reveal that the interfacial electric field built in the heterojunction accelerates the photogenerated electrons transfer from MoS<sub>2</sub> to COF under light irradiation, greatly facilitating charge separation and transfer and thus enhancing the activity and C<sub>2</sub>H<sub>6</sub> selectivity for CO<sub>2</sub> photoreduction. The optimized MoS<sub>2</sub>@COF-15 achieves C<sub>2</sub>H<sub>6</sub> production rate up to 56.2 μmol·g<sup>-1</sup>·h<sup>-1</sup> with 83.8% of selectivity, which is about 8.6 and 31.2 times higher than that of pristine MoS<sub>2</sub> and COF under identical conditions. The in-situ DRIFTS and DFT calculations indicate that the structure of MoS<sub>2</sub>@COF composite can promote the adsorption of \*CO and the formation of \*COCO, facilitating C-C coupling to convert into C<sub>2</sub>H<sub>6</sub> product.

### 1. Introduction

The solar-driven carbon dioxide (CO<sub>2</sub>) photoreduction into valuable hydrocarbons has been regarded as one of the most attractive ways to alleviate the greenhouse effect and energy shortages [1,2]. However, the inertness of liner CO<sub>2</sub> molecules and multiple proton-coupled electrons transfer steps pose great challenges related to the reaction activity and product selectivity [3]. Among all the possible products of CO<sub>2</sub> reduction, C<sub>2+</sub> products such as ethane (C<sub>2</sub>H<sub>6</sub>) are more desirable ones because of higher energy density and economic values [4]. Nevertheless, most examples of photocatalytic CO<sub>2</sub> reduction reported currently mainly produced C<sub>1</sub> products (e.g., CO, CH<sub>4</sub>, and HCOOH, etc.); in contrast, preferred high-value C<sub>2+</sub> products were rarely achieved due to multielectron steps and sluggish kinetics for C-C coupling formation [5–7]. In particular, the conversion of CO<sub>2</sub> to C<sub>2</sub>H<sub>6</sub> is more complex, involving 14-electron reaction process and the formation of many intermediates, which has a high activation energy barrier, resulting in lower efficiency and product selectivity [8–11]. Although considerable research efforts have been devoted to improving CO<sub>2</sub> reduction kinetics and tailoring product distribution, the photoreduction efficiency and product selectivity are still far from satisfactory. Therefore, it is imperative to explore effective photocatalysts to simultaneously improve the

efficiency and selectivity of photocatalytic CO<sub>2</sub> reduction to C<sub>2+</sub> products, and a detailed understanding of the reaction mechanism also needs to be further clarified.

In recent years, covalent organic frameworks (COFs) have shown great potential in photocatalysis since the unique π-stacked structure endows them with defined pathways for charge carrier transfer or high photoconductivity [12,13]. Moreover, intrinsic characteristics of high surface area, tunable porosity and structural designability have also enabled COFs to show superior potential for CO<sub>2</sub> adsorption, diffusion, and activation [14]. Benefiting from these advantages, various COFs have been developed as photocatalysts for photocatalytic CO<sub>2</sub> reduction thus far [15–22]. It is worth mentioning that some COFs under visible light irradiation have been proven to be superior concerning traditional amorphous polymers and inorganic semiconductors. However, an undeniable fact is that the photocatalytic activity can hardly be further improved only by tuning their structures and band gaps because of the high recombination rate of photogenerated electron-hole pairs in single-component COFs [23,24]. Thus, how maximizing the photocatalytic activity of COFs still faces enormous challenges.

Recent studies demonstrated that integrating semiconductors with proper band positions into COFs to construct inorganic-organic hybrid composites is an effective solution to enhance photogenerated charge

\* Corresponding authors.

E-mail addresses: [lanxingwang@hbu.edu.cn](mailto:lanxingwang@hbu.edu.cn) (X. Lan), [baiguoyi@hotmail.com](mailto:baiguoyi@hotmail.com) (G. Bai).

<sup>1</sup> These authors contributed equally to this work

separation efficiency [25,26]. Various hybridization of COFs with other functional materials, including transition metal sulfides (e.g., CdS and FeS<sub>2</sub>) [27–29], metal oxides (e.g., TiO<sub>2</sub>, Bi<sub>2</sub>WO<sub>6</sub>, and  $\alpha$ -Fe<sub>2</sub>O<sub>3</sub>) [30–32], metal-organic frameworks (MOFs) [33–36], and graphitic carbon nitride (g-C<sub>3</sub>N<sub>4</sub>) [37–39], have been developed and successfully applied for photocatalysis in the past decades. More importantly, the multi-component interfaces can modulate the electronic structures of photocatalysts and facilitate charge transfer and separation through the interfacial electric field, which results in a high electron density at catalytic sites, thereby presenting a superior performance in photocatalytic reactions [40,41]. Despite that, the key factors influencing catalytic efficiency are largely unknown in hybrid composites. Thus, it is still highly desirable to rationally construct COFs-based multicomponent composites with high activity for CO<sub>2</sub> photoreduction and uncover the photocatalytic mechanism.

Herein, we reported the hybridization of COFs with amino-modified molybdenum sulfide (MoS<sub>2</sub>) to construct covalently integrated MoS<sub>2</sub>@COF hybrid composites, in which the anthraquinone-based covalent organic framework was chosen to construct the heterostructure. The experimental and theoretical calculation results indicated that there was strong electron interaction between MoS<sub>2</sub> and COF to facilitate the separation and transfer of interfacial charge, such that it consequently contributed to the superior photocatalytic CO<sub>2</sub> reduction activity under visible light irradiation. Photocatalytic results demonstrated that the MoS<sub>2</sub>@COF composites could accelerate multielectron reduction to produce C<sub>2+</sub> hydrocarbons, especially C<sub>2</sub>H<sub>6</sub>, with high selectivity. With the resulting a series of MoS<sub>2</sub>@COF composites, the highest C<sub>2</sub>H<sub>6</sub> production rate under visible light reached up to 56.2  $\mu\text{mol}\cdot\text{g}^{-1}\cdot\text{h}^{-1}$ , which was 8.6 and 31.2 times that of pure MoS<sub>2</sub> and COF, respectively. The possible photocatalytic reaction mechanisms of CO<sub>2</sub> reduction were proposed on the basis of the in-situ spectra. This work highlights the interfacial engineering of the MoS<sub>2</sub>@COF hybrid composites, which provides an impressive strategy to facilitate CO<sub>2</sub> conversion to C<sub>2+</sub> hydrocarbons.

## 2. Experimental section

### 2.1. Materials

1,3,5-Triformylphloroglucinol (Tp, 97%) was obtained from Jilin Chinese Academy of Sciences-Yanshen Technology Co., Ltd. 2,6-Diaminoanthraquinone (DAAQ, 97%) was purchased from Shanghai Bide Pharmatech Co., Ltd. Tris(2,2'-bipyridine)ruthenium(II) chloride hexahydrate ([Ru(bpy)<sub>3</sub>]Cl<sub>2</sub>·6H<sub>2</sub>O) was purchased from Shanghai Haohong Pharmatech Technology Co., Ltd. Sodium molybdate (Na<sub>2</sub>MoO<sub>4</sub>·2H<sub>2</sub>O, 99%) was purchased from Energy Chemical Co., Ltd. Extra pure mesitylene was purchased from J&K Scientific Co., Ltd. Ethylenediamine anhydrous (EDA, 99.5%), triethanolamine (TEOA, 99.5%), thiourea (CH<sub>4</sub>N<sub>2</sub>S, 99%), glacial acetic acid (CH<sub>3</sub>COOH, 99.5%) and other common solvents were provided from local chemical suppliers. All the reagents are analytical grade and used without further purification prior to use.

### 2.2. Preparation of photocatalysts

#### 2.2.1. Preparation of MoS<sub>2</sub> nanoflowers

The MoS<sub>2</sub> nanoflowers were synthesized through the traditional hydrothermal approach according to previous literatures with a slight modification [42]. Typically, 30 mL of EDA was slowly injected into 30 mL deionized water and continuously stirred for 0.5 h. Afterwards, 0.484 g of Na<sub>2</sub>MoO<sub>4</sub>·2H<sub>2</sub>O and 0.762 g of thiourea were dissolved into the solution, which was further stirred for 15 min at room temperature and then transferred into a Teflon-lined stainless steel autoclave, heated at 200 °C for 24 h, and then air-cooled to room temperature. After the hydrothermal treatment completed, the obtained precipitate was filtered and sequentially washed with deionized water and ethanol for

several times, respectively, and dried at 60 °C for overnight under vacuum, finally yielding the amino-functional MoS<sub>2</sub> nanoflowers.

#### 2.2.2. Synthesis of MoS<sub>2</sub>@COFs hybrid composites

The MoS<sub>2</sub>@COFs hybrid composites was obtained through two steps as follows. Firstly, 50 mg amino-functional MoS<sub>2</sub> and 50 mg 1,3,5-triformylphloroglucinol (TFP) were added to 20 mL DMF and then dispersed ultrasonically for 0.5 h. Subsequently, 0.2 mL 6 M CH<sub>3</sub>COOH aqueous solution was added into the above solution stirred for 12 h at 50 °C. The obtained black solid was washed twice with acetone and dried at 60 °C for overnight under vacuum oven, referred to as MoS<sub>2</sub>(CHO). Second, the obtained MoS<sub>2</sub>(CHO) (5, 10, 15 and 20 mg), Tp (60 mg), DAAQ (102 mg), and DMAc/mesitylene (3/1 v/v, 3.6 mL) were added into a Schleck-flask (15 mL). After the slurry was sonicated for 30 min at room temperature, 6 M acetic acid (0.2 mL) was added into the mixture. Then, the Schleck-flask was degassed by three freeze-pump-thaw cycles, sealed off under vacuum, and heated at 120 °C for 3 days. After completion, the resulting red precipitate was collected by filtration and washed successively with *N,N*-dimethyl formamide and acetone for several times, and then dried at 60 °C under vacuum for 24 h to obtain red power, referred as the MoS<sub>2</sub> @COF-n (n represents the amount of MoS<sub>2</sub>(CHO) added). In addition, for comparation, the pure COF was prepared by the same procedure except for without the MoS<sub>2</sub>(CHO).

### 2.3. Photocatalytic CO<sub>2</sub> reduction

The photoreduction CO<sub>2</sub> experiments were performed in a custom reaction reactor at ambient temperature and atmospheric pressure. A 300 W xenon lamp (PLS-SXE 300, Beijing Perfectlight Co. Ltd.) with a 420 nm-cut filter to cut off UV light (420–780 nm) was used as light source, which was positioned 10 cm away from the reactor. The focused intensity on the flask was ca. 209 mW/cm<sup>2</sup>. In a typical process, photocatalyst (1.0 mg) and [Ru(bpy)<sub>3</sub>]Cl<sub>2</sub>·6 H<sub>2</sub>O (5.0 mg) were dispersed into a mixed solution of acetonitrile (3.0 mL), deionized water (1.0 mL) and triethanolamine (1.0 mL), and the mixture was then ultrasonic for 10 min to form a homogeneous suspension solution. Prior to irradiation, the reaction system was filled with high-purity CO<sub>2</sub> (99.999%) for 5 min, repeated several times to exclude residual air in the reactor. Subsequently, the reactor was sealed and the light was turned on circulating cold water bath system, and the reaction system was maintained at 25 °C during photocatalytic reactions. The products of the CO<sub>2</sub> photocatalytic reduction were analyzed by gas chromatography equipped with thermal-conductive detector (TCD) and flame-ionization detector (FID) (GC9790II plus, Fuli Analytical Instrument Co., Ltd.). Isotope-labeled experiments were conducted with <sup>13</sup>CO<sub>2</sub> instead of <sup>12</sup>CO<sub>2</sub> and D<sub>2</sub>O instead of H<sub>2</sub>O under the same condition and the obtained gaseous products were analyzed by a GC-MS.

## 3. Results and discussion

### 3.1. Material synthesis and characterizations

The MoS<sub>2</sub>@COF heterostructures were constructed via a facile in-situ synthetic process as illustrated in Fig. 1a. Briefly, MoS<sub>2</sub> was first synthesized using ethylenediamine as solvent through the previously reported solvothermal method with slight modification [42]. The NH<sub>2</sub> groups in as-synthesized MoS<sub>2</sub> can direct the sequent formation of COF through chemical reactions [33]. Fourier transformed infrared (FT-IR) spectroscopy shows a typical NH<sub>2</sub> stretching band at 3100–3300 cm<sup>-1</sup>, indicating that NH<sub>2</sub> groups are successfully grafted on the surface (Fig. S1). Powder X-ray diffraction (PXRD) pattern of the aforementioned MoS<sub>2</sub> exhibit broad peaks at 17° and 33°, which are attributed to the (002) and (100) planes of hexagonal MoS<sub>2</sub> phase (Fig. S2) [43–45]. Then, the resulting MoS<sub>2</sub> @COF composites were synthesized by introducing a certain amount of MoS<sub>2</sub>(CHO), the surface functionalization of MoS<sub>2</sub> with 1,3,5-triformylphloroglucinol (Tp), into the reaction system

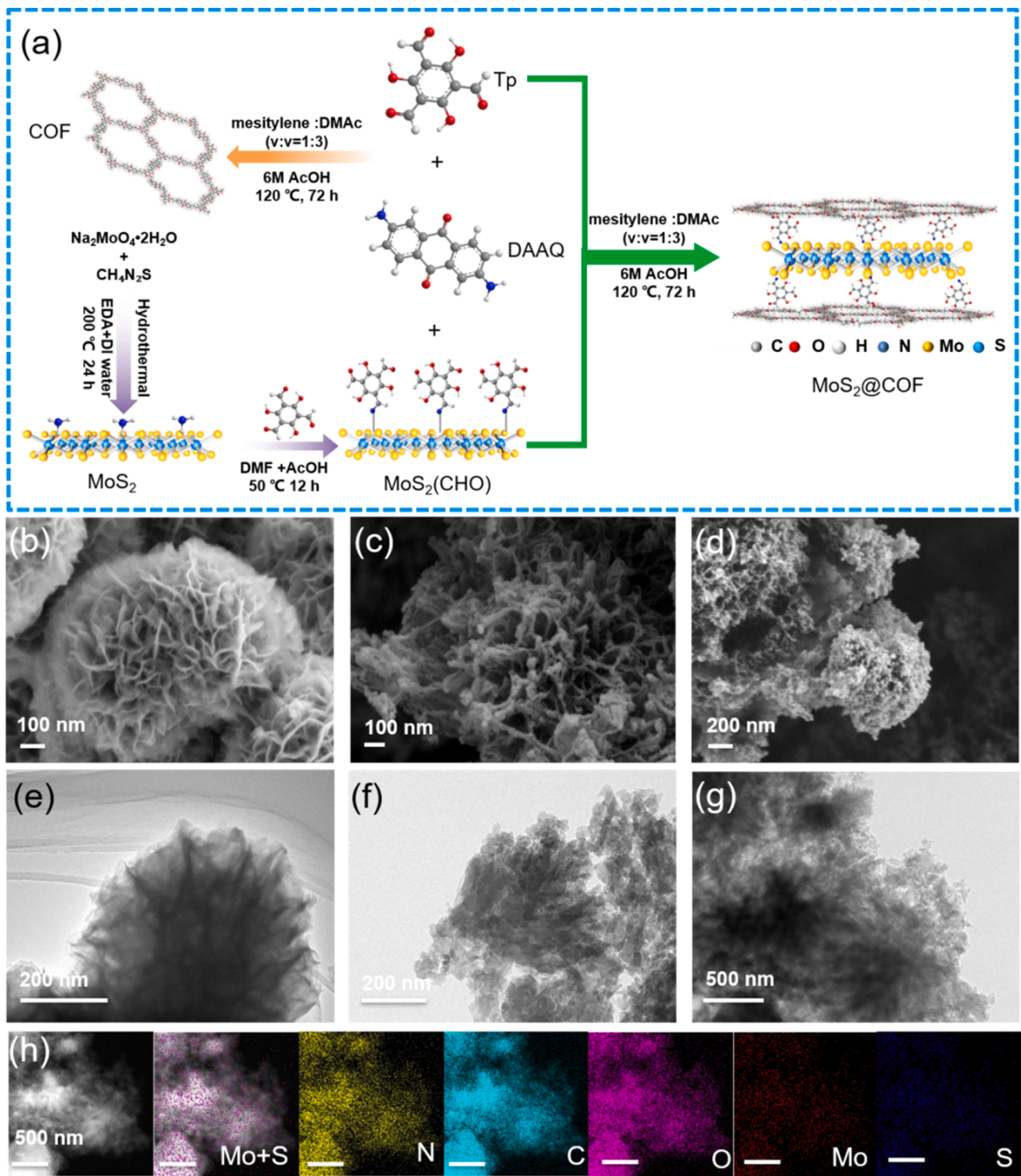


**Fig. 1.** (a) Schematic illustration of the synthesis of MoS<sub>2</sub>@COF composites. SEM images of (b) MoS<sub>2</sub>, (c) COF and (d) MoS<sub>2</sub>@COF-15. TEM images of (e) MoS<sub>2</sub>, (f) COF and (g) MoS<sub>2</sub>@COF-15. (h) EDX elemental mapping of MoS<sub>2</sub>@COF-15.

of constructing COF assembled from Tp and 2,6-diaminoanthraquinone (DAAQ) in *N,N*-dimethylformamide (DMF) by an acid-catalyzed condensation reaction. The same protocol was employed to synthesize a series of MoS<sub>2</sub>@COF composites by adding different amounts of MoS<sub>2</sub>, namely MoS<sub>2</sub>@COF-5, MoS<sub>2</sub>@COF-10, MoS<sub>2</sub>@COF-15, MoS<sub>2</sub>@COF-20 according to the amounts added of MoS<sub>2</sub>, to maximize the reactivity.

The morphologies of as-synthesized MoS<sub>2</sub>, COF and representative MoS<sub>2</sub>@COF-15 composite were observed by scanning electron microscopy (SEM) and transmission electron microscope (TEM). Pristine MoS<sub>2</sub>

presents a hierarchical flower-like morphology formed by self-assembly interweaving sheets with a diameter of approximately 500 nm (Fig. 1b, e), whilst COF shows a fibrous and flexuous morphology (Fig. 1c, f). The obtained MoS<sub>2</sub>@COF-15 composite displays a similar morphology to COF (Fig. 1d, g). The TEM image of MoS<sub>2</sub>@COF-15 further demonstrates that the flower-like MoS<sub>2</sub> is compactly wrapped in a thick layer of fibrous COF. The EDX elemental mapping results confirm the uniform distribution of C, N, O, Mo and S elements throughout the entire framework (Fig. 1h). SEM and TEM analyses verify the successful

preparation of the core-shell  $\text{MoS}_2@\text{COF}$ .

$\text{N}_2$  adsorption-desorption experiments at 77 K were conducted for  $\text{MoS}_2$ , COF and  $\text{MoS}_2@\text{COF-15}$  to assess their permanent porosity as presented in Fig. 2a. Both the isotherms of COF and  $\text{MoS}_2@\text{COF-15}$  composite exhibit the reversible type I isotherms with H3 hysteresis loop, while the  $\text{MoS}_2$  exhibits type IV isotherm, which is assigned to the stacking holes caused by aggregating particles. The Brunauer-Emmett-Teller (BET) surface area of  $\text{MoS}_2@\text{COF-15}$  was calculated to be  $731.3 \text{ m}^2 \cdot \text{g}^{-1}$ , which is lower than that of pristine COF ( $945.4 \text{ m}^2 \cdot \text{g}^{-1}$ ) (Table S1). Furthermore, the pore size distribution curves show that their pore width is centered at relatively narrow distributions of about 1.7 nm (Fig. S3). However, the pure  $\text{MoS}_2$  almost has no pore channels with surface area of only  $12.0 \text{ m}^2 \cdot \text{g}^{-1}$ . These results suggest that the integration of  $\text{MoS}_2$  in the COF has no significant influence on the morphology and porosity, further reflecting the formation of core-shell structure. The XRD patterns were recorded to probe the crystal structure of the as-prepared samples as shown in Fig. 2b. The pristine COF exhibits characteristic diffraction peaks at  $3.5^\circ$ ,  $5.8^\circ$  and  $26.9^\circ$ , corresponding to (100), (110) and (001) planes, respectively [46]. The XRD patterns of  $\text{MoS}_2@\text{COF}$  composites exclusively possess the diffraction peaks of COF but no obvious peaks belonging to  $\text{MoS}_2$  due to the low loading content. It is worth noting that the (100) plane peak intensity of COF gradually decreases with the increase of  $\text{MoS}_2$  component. Furthermore, the FT-IR spectrum of COF reveals the obvious appearance of C-N stretching band at  $1250 \text{ cm}^{-1}$  and the disappearance of N-H stretching band in the 2,6-diaminoanthraquinone, indicating the formation of COF (Fig. S4). The FT-IR spectrum of  $\text{MoS}_2@\text{COF}$  agrees well with COF and hardly visible peaks of  $\text{MoS}_2$ . Solid-state  $^{13}\text{C}$  CP-MAS NMR spectra were collected for the pure COF and  $\text{MoS}_2@\text{COF-15}$ . Both the COF and  $\text{MoS}_2 @\text{COF-15}$  exhibit distinctive resonance peaks at 182, 143, and 108 ppm, corresponding to the carbons in  $\text{C=O}$ ,  $\text{C-N}$  and  $\text{C=C}$  bonds in the keto-amine form (Fig. S5). The similar spectra reveal that the incorporation of  $\text{MoS}_2$  in the synthesis process does not disturb the synthesis and its structure of COF. The actual content of Mo in  $\text{MoS}_2@\text{COF-15}$  is 3.84 wt% determined by inductively coupled plasma-mass spectrometry (ICP-MS).

To figure out the electronic interaction between  $\text{MoS}_2$  and COF-15, in-situ irradiated X-ray photoelectron spectroscopy (XPS) was carried out for the  $\text{MoS}_2$ , COF and  $\text{MoS}_2 @\text{COF-15}$ . The survey scan of the  $\text{MoS}_2@\text{COF-15}$  sample in Fig. S6 reveals the coexistence of C, N, O, Mo and S elements, which is in accordance with the EDX results, further verifying the formation of heterojunction materials. As shown in Fig. 3a and b, in comparison with pristine  $\text{MoS}_2$ , the XPS binding energy of Mo 3d and S 2p of  $\text{MoS}_2@\text{COF-15}$  composite obviously shifts towards lower binding energy in darkness, indicating an increase in the electron

density of  $\text{MoS}_2$ . In contrast, compared with the pure COF, the binding energies of O 1s in  $\text{MoS}_2@\text{COF-15}$  composite shift to higher energy levels in darkness, implying that the electrons spontaneously transfer from COF to  $\text{MoS}_2$  (Fig. 3c). Nevertheless, the C 1s and N 1s XPS binding energy did not exhibit similar phenomena to the O 1s XPS (Fig. 3d and S7). Furthermore, compared with  $\text{MoS}_2@\text{COF-15}$  in darkness, the binding energies of Mo 3d and S 2p in  $\text{MoS}_2@\text{COF-15}$  composite under light irradiation significantly shift to higher energy levels, while the binding energies of O 1s in  $\text{MoS}_2@\text{COF-15}$  composite move to lower energy levels, suggesting the photogenerated electrons transfer from  $\text{MoS}_2$  to COF under light irradiation [47,48]. These XPS results suggest the  $\text{MoS}_2$  component actually acts as the electron acceptor without illumination but electron donor under illumination in  $\text{MoS}_2@-\text{COF}$ , and provide important evidence for the charge transfer pathway across the heterojunction interface under light irradiation [49].

Density functional theory (DFT) calculations were performed to further reveal the charge transfer in the  $\text{MoS}_2@\text{COF-15}$  heterojunction photocatalyst. As shown in Fig. 4a and b, the work functions of  $\text{MoS}_2$  and COF were calculated to be about 5.94 and 5.73 eV, respectively, revealing that electrons in COF can transfer to  $\text{MoS}_2$  via the heterojunction interface driven by the potential difference until the Fermi energy is equilibrated [50]. This result can be directly proved by charge density difference and planar-averaged electron density difference as illustrated in Fig. 4c and S8. Strikingly, charge redistribution mainly appears near the interface; moreover, the electrons accumulate near the  $\text{MoS}_2$  layer, while holes accumulate near the COF layer. The spontaneous charge transfer through the interfacial between  $\text{MoS}_2$  and COF is the staple cause for triggering the induced built-in electric field [51]. Combined with in-situ XPS and theoretical calculation results, the charge transfer mechanism of the  $\text{MoS}_2@\text{COF-15}$  heterojunction is depicted in Fig. 4d-f. Since the COF has a higher Fermi level than that of  $\text{MoS}_2$ , after the contact of  $\text{MoS}_2$  and COF in darkness, the electrons of the COF spontaneously flow to  $\text{MoS}_2$  until achieving the same Fermi energy level and forming the stable built-in electric field (Fig. 4d). During the process of electron migration, the interface region of COF component is positively charged owing to losing electrons, while the interface region of  $\text{MoS}_2$  is negatively charged due to acquiring electrons, giving rise to upward bend of band edge of COF and downward that of  $\text{MoS}_2$  (Fig. 4e). Under illumination, both  $\text{MoS}_2$  and COF are photoexcited to produce electrons and holes. The built-in electric field enables the transfer of photogenerated electrons accumulated in  $\text{MoS}_2$  to COF to recombine with the photogenerated holes (Fig. 4f), revealing that the interfacial charge transfer within the heterojunction possibly conforms to Z-scheme (S-scheme) mechanism [52]. Meanwhile, the photogenerated holes and electrons are maintained on valent band of  $\text{MoS}_2$  and the conduction

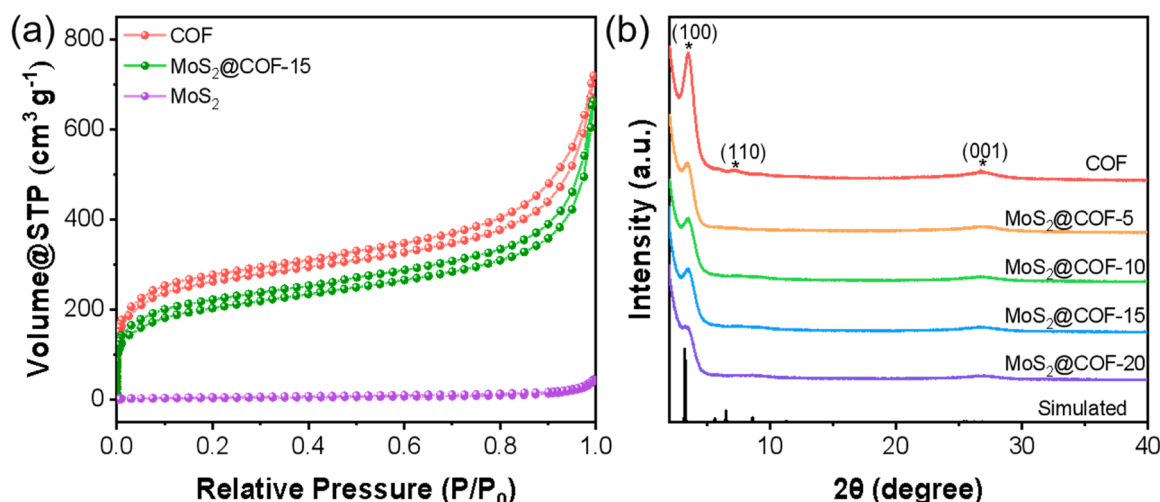
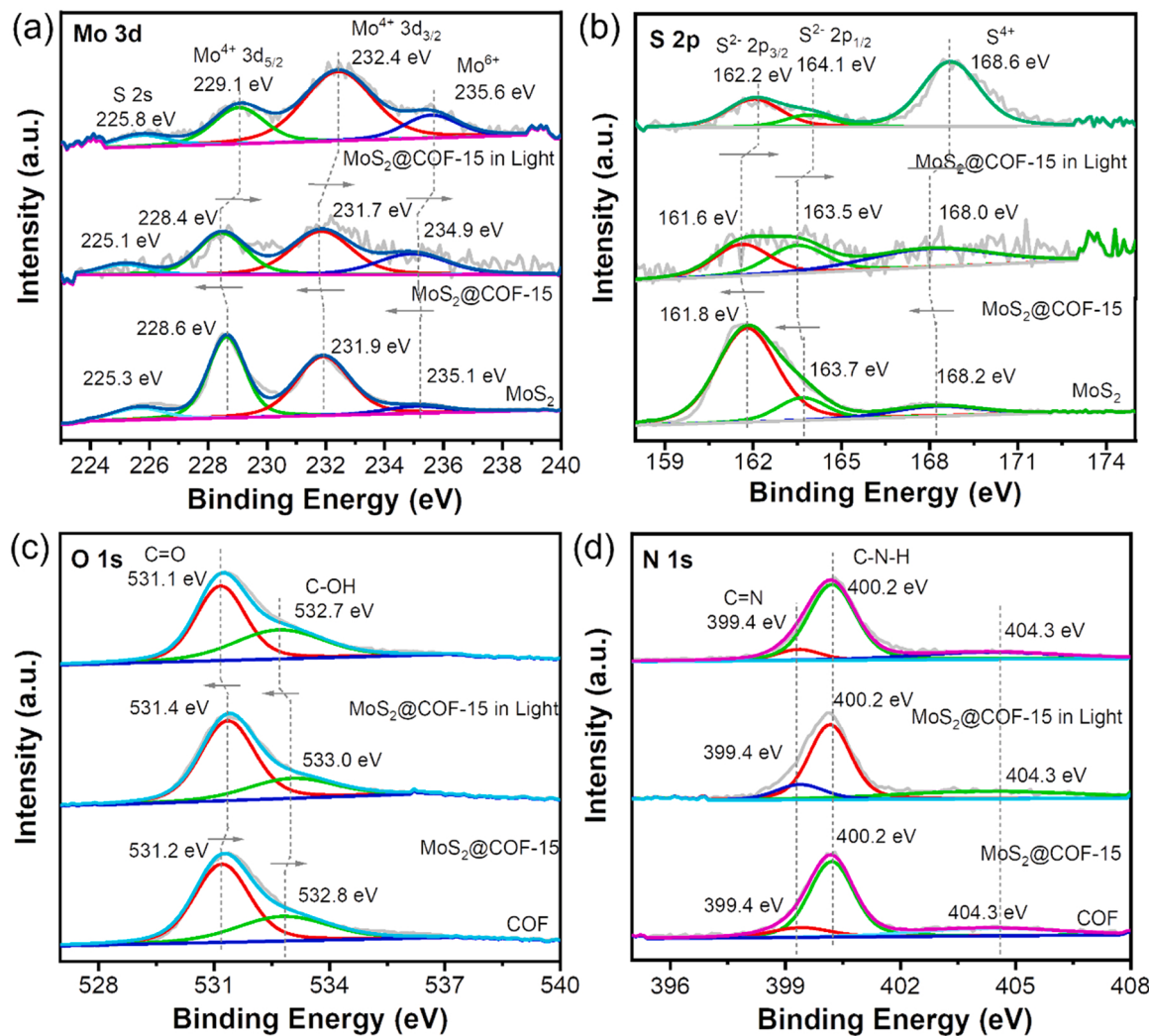


Fig. 2. (a)  $\text{N}_2$  adsorption-desorption isotherms of  $\text{MoS}_2$ , COF and  $\text{MoS}_2@\text{COF-15}$  at 77 K. (b) XRD patterns of COF and  $\text{MoS}_2@\text{COFs}$ .



**Fig. 3.** *In-situ* XPS spectra of (a) Mo 3d, (b) S 2p, (c) O 1s, and (d) N 1s in pristine MoS<sub>2</sub>, COF, and MoS<sub>2</sub>@COF-15 samples tested in darkness and under illumination ( $\lambda = 300\text{--}2000\text{ nm}$ ).

band of COF, respectively, which will participate in the photocatalytic CO<sub>2</sub> reaction.

### 3.2. Optical properties and charge transfer dynamics

The photoelectric properties of MoS<sub>2</sub>, COF and MoS<sub>2</sub>@COFs were then investigated to assess light absorption, charge separation and surface reactions. The optical absorption behaviors of these samples were first explored by ultraviolet-visible diffuse reflectance spectra (UV-vis DRS). As shown in Fig. 5a, pure COF exhibited strong absorption in visible light region with an absorption edge at 800 nm, while bare MoS<sub>2</sub> presented light absorption in the almost full spectrum owing to its black surface [49]. Compared with pure COF, the light absorption edge of MoS<sub>2</sub>@COFs only occurred a slight blue shift, indicating that the great upgrade in the photocatalytic activity of MoS<sub>2</sub>@COFs was not ascribed to the change of light absorption. Additionally, the optical bandgap (E<sub>g</sub>) of MoS<sub>2</sub>, COF and MoS<sub>2</sub>@COF-15 were calculated to be about 1.91, 1.69 and 1.87 eV by using Tauc plots analysis, respectively (Fig. S9). Furthermore, Mott-Schottky measurements were performed to determine the conduction band minimum (CBM) potentials of the samples (Fig. S10). The flat band potential (E<sub>fb</sub>) of MoS<sub>2</sub> and COF was calculated to be  $-1.11$  and  $-1.44$  V (vs. Ag/AgCl, pH = 7), that is,  $-0.91$  and  $-1.24$  V (vs. NHE, pH = 7), respectively. It is known that CBM potential of the n-type semiconductor is typically more negative by approximately

0.1 V than the flat-band potential [53,54]. Therefore, CBM potentials of pure MoS<sub>2</sub> and COF were calculated to be  $-1.01$  and  $-1.34$  V (NHE). The valence band maximum (VBM) positions of pure MoS<sub>2</sub> and COF were situated at 0.90 and 0.53 V, respectively. In this case, the band structures of MoS<sub>2</sub> and COF can be summarized in Fig. S11.

To unveil the photogenerated charge transfer behavior, steady-state photoluminescence (PL) spectra, time-resolved photoluminescence decay (TRPL) spectra and electrochemical measurements were investigated for these samples. As shown in Fig. 5b, the PL intensities of MoS<sub>2</sub>@COFs composites were greatly decreased with respect to pure COF, implying that the heterojunction might largely suppress the recombination of photogenerated carriers. Among all of the samples, the MoS<sub>2</sub>@COF-15 exhibited the weakest PL intensity, confirming the superior charge separation and migration ability. The average PL lifetime increased from 1.15 ns for COF to 2.46 ns for MoS<sub>2</sub>@COF-15 (Fig. 5c), which was mainly attributed to the interfacial charge transfer between MoS<sub>2</sub> and COF in the heterojunction. An improved charge separation efficiency was also confirmed by electrochemical impedance spectra (EIS) and transient photocurrent response. It is noted that the EIS Nyquist plots of the MoS<sub>2</sub>@COF-15 possessed a semicircle with the smallest radius than other samples (Fig. 5d), signifying the best charge conductivity and carrier transport capacity [55]. The higher transient photocurrent response of MoS<sub>2</sub>@COF-15 further illustrated that constructing a heterostructure is much more conducive to promoting

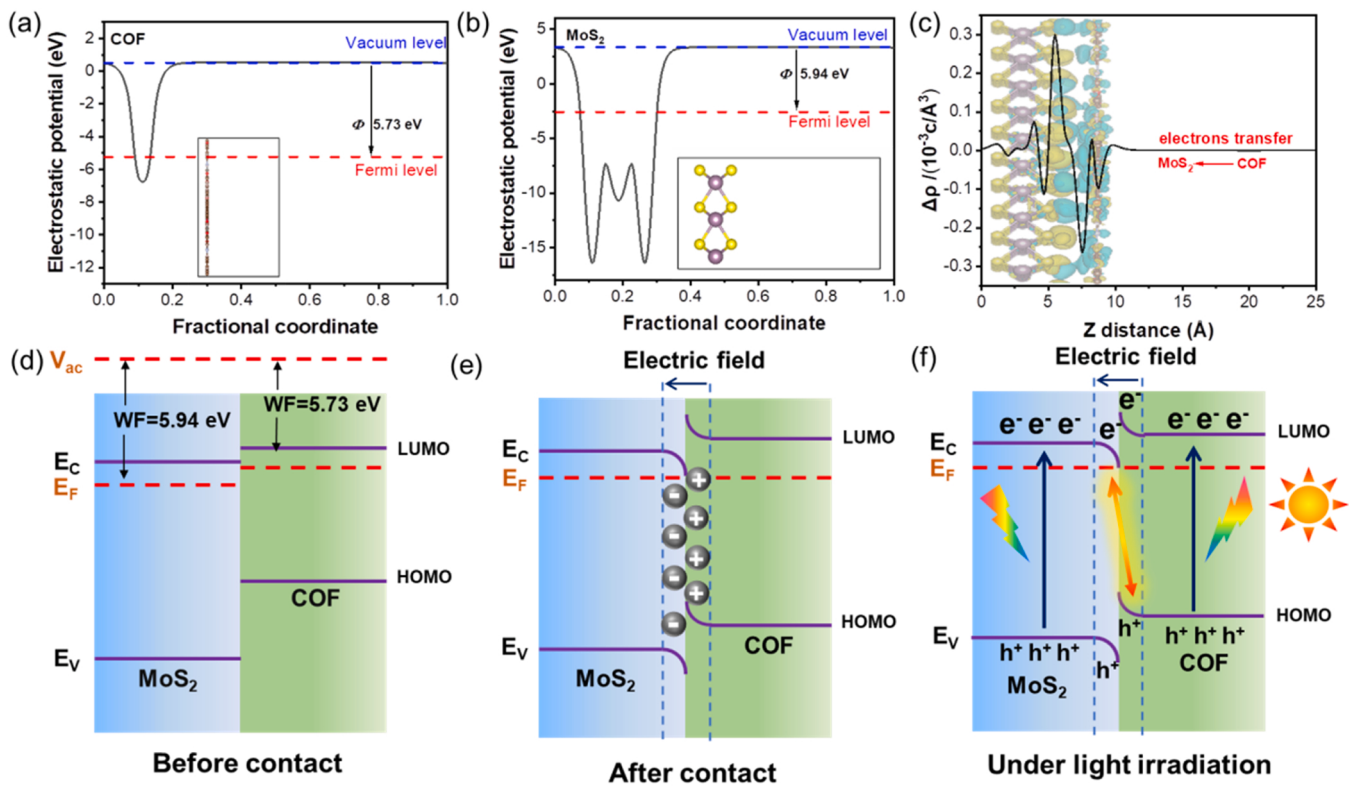


**Fig. 4.** The calculated work functions of (a) COF and (b) MoS<sub>2</sub>. (c) The planar averaged charge density difference  $\Delta\rho$  along the Z-direction for the MoS<sub>2</sub>@COF-15 (The insert represents the 3D differential charge density map for the MoS<sub>2</sub>@COF-15). Schematic illustration of the relative band positions and charge transfer process of COF and MoS<sub>2</sub> (d) before contact, (e) after contact and (f) under light irradiation.

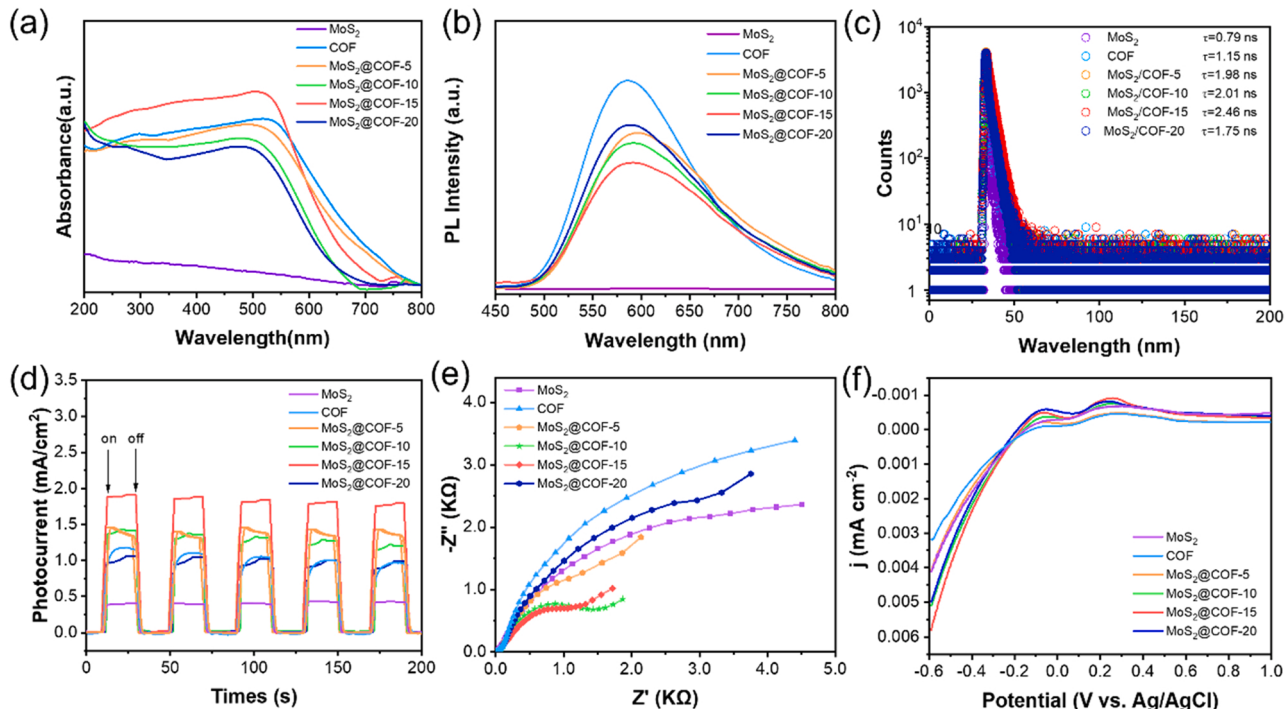


**Fig. 5.** (a) UV-vis DRS spectra, (b) steady-state PL emission spectra, (c) TRPL spectra, (d) EIS Nyquist plots, (e) I-t curves, and (f) LSV curves in CO<sub>2</sub> atmosphere in darkness and under light illumination of MoS<sub>2</sub>, COF and MoS<sub>2</sub>@COFs composites.

electron transfer between two semiconducting phases (Fig. 5e). In addition, linear sweep voltammetry (LSV) measurements were also carried out over the MoS<sub>2</sub>, COF and MoS<sub>2</sub>@COFs composites as

electrodes in the CO<sub>2</sub>-saturated KHCO<sub>3</sub> solution (Fig. 5f). After bubbling CO<sub>2</sub> into the electrolyte solution, a higher cathodic current was observed for MoS<sub>2</sub>@COF-15 electrode, indicative of the higher CO<sub>2</sub>

photoreduction activity of the  $\text{MoS}_2@\text{COF-15}$  composite [56,57]. By combining these results, it can be reasonably deduced that the heterostructure with strong electron coupling effect dramatically stimulates charge separation and interfacial charge transfer under the action of interfacial electric field.

### 3.3. Photocatalytic performance $\text{CO}_2$ reduction

The activities of photocatalytic  $\text{CO}_2$  reduction performance of as-obtained photocatalysts were evaluated by using  $[\text{Ru}(\text{bpy})_3]\text{Cl}_2 \cdot 6\text{H}_2\text{O}$  as photosensitizer and triethanolamine (TEOA) as hole-scavenger in an acetonitrile/water ( $\text{CH}_3\text{CN}/\text{H}_2\text{O}$ ) mixed solution under visible light irradiation. As shown in Fig. 6a and b, the main products were  $\text{CO}$ ,  $\text{CH}_4$ , and  $\text{H}_2$  over the pure  $\text{MoS}_2$ , achieving generation rates of 80.6, 123.2, and  $721.0 \mu\text{mol} \cdot \text{g}^{-1} \cdot \text{h}^{-1}$  respectively; besides, further reduced products  $\text{C}_{2+}$  hydrocarbons,  $\text{C}_2\text{H}_4$  and  $\text{C}_2\text{H}_6$  with generation rates being 1.7 and  $6.5 \mu\text{mol} \cdot \text{g}^{-1} \cdot \text{h}^{-1}$ , were also detected (Figs. S12, S13). No liquid products could be detected from the Nuclear Magnetic Resonance (NMR) spectra after photocatalytic tests (Fig. S14). In contrast, the pure COF presented an inferior activity, but  $\text{H}_2$  was not generated, suggesting its high selectivity toward  $\text{CO}_2$  reduction. More interestingly, the  $\text{MoS}_2@\text{COF}$  hybrid composites could provide notable selectivity toward  $\text{C}_2\text{H}_6$  production. In particular, the  $\text{MoS}_2@\text{COF-15}$  showed the highest rates for  $\text{C}_2\text{H}_6$  production ( $56.2 \mu\text{mol} \cdot \text{g}^{-1} \cdot \text{h}^{-1}$ ), which was 8.6 and 31.2 times higher than those of pure  $\text{MoS}_2$  and COF, whereas the generation rates for  $\text{CO}$  and  $\text{CH}_4$  were decreased simultaneously. Meanwhile, the product selectivity of  $\text{C}_2\text{H}_6$  (83.8%) was also significantly improved, which was more than 27.9 and 7.4 times higher than that for pure  $\text{MoS}_2$  and COF, respectively (Fig. 6c). These results indicated that the COF component might have a great contribution to the production of  $\text{C}_2\text{H}_6$  over the  $\text{MoS}_2@\text{COFs}$ . The enhanced activity and selectivity of  $\text{MoS}_2@\text{COF}$  towards the production of  $\text{C}_2\text{H}_6$  was possibly ascribed to the increased  $\text{CO}_2$  adsorption and higher density of photogenerated electrons, thereby reducing the reaction barrier and stabilizing the  $\text{CO}$  intermediates moderately. Of note, the photocatalytic performance of  $\text{MoS}_2@\text{COF-15}$

in  $\text{C}_2\text{H}_6$  evolution was also competitive compared with previously reported photocatalysts (Table S2). In addition, the mixture of 15%  $\text{MoS}_2$  and 85% COF (named as  $\text{MoS}_2+\text{COF}$ ) also exhibited a remarkably enhanced  $\text{C}_2\text{H}_6$  production rate ( $26.5 \mu\text{mol} \cdot \text{g}^{-1} \cdot \text{h}^{-1}$ ) compared with the pure samples, but which was obviously lower than that of  $\text{MoS}_2@\text{COF-15}$ . These results testified that the rational construction of  $\text{MoS}_2@\text{COF}$  heterostructures could significantly promote  $\text{CO}_2$  conversion to  $\text{C}_2\text{H}_6$  and suppress competitive hydrogen evolution reaction. Moreover, the apparent quantum yield (AQY) of  $\text{MoS}_2@\text{COF-15}$  achieved the highest value 0.03% for the photocatalytic  $\text{CO}_2$  reduction with monochromatic light at 450 nm (Fig. S15a), which is 7.5 and 2.3 times higher than that of pure  $\text{MoS}_2$  and COF (Fig. S15b). The comparative AQY values at the stationary point strongly reveal the superior activity of  $\text{MoS}_2@\text{COF-15}$ , which is believed that the high AQY is ascribed to high charge separation efficiency and carrier mobility in the heterojunction.

Several control experiments were carried out for  $\text{MoS}_2@\text{COF-15}$  including testing without catalyst, photosensitizer, hole-scavenger, and testing with the catalyst but in the dark or without  $\text{CO}_2$  but in Ar under otherwise same reaction conditions. As shown in Fig. 6d, no detectable amount of  $\text{C}_2\text{H}_6$  was produced in all these cases, indicating their indispensable contributions to the production of  $\text{C}_2\text{H}_6$ . Nevertheless, the production of  $\text{CO}$  and  $\text{CH}_4$  might be observed, especially only with  $[\text{Ru}(\text{bpy})_3]\text{Cl}_2$  but without catalyst, which suggested that the photosensitizer could act as a catalyst for  $\text{CO}_2$  reduction to  $\text{CO}$ . Furthermore, a small amount of  $\text{CO}$  and  $\text{CH}_4$  product were observed in Ar atmosphere, but their yields were far lower than that under  $\text{CO}_2$  atmosphere. The  $\text{C}_1$  products could be attributed to residual  $\text{CO}_2$  after Ar purging because the  $\text{CO}_2$  chemisorbed on the photocatalyst surface was difficult to be completely removed under ambient conditions [58]. Thus, it was not surprising that a small amount of  $\text{CO}$  and  $\text{CH}_4$  could be produced but almost no  $\text{C}_2\text{H}_6$ . Moreover, no any  $\text{CO}_2$  products were observed in the darkness. These results unambiguously illustrated that  $\text{C}_2\text{H}_6$  really originated from the photocatalytic  $\text{CO}_2$  reduction reaction rather than carbon contamination [59]. Moreover, the isotope labeling experiment was conducted by using  $^{13}\text{CO}_2$  instead of  $^{12}\text{CO}_2$  gas to further verify the

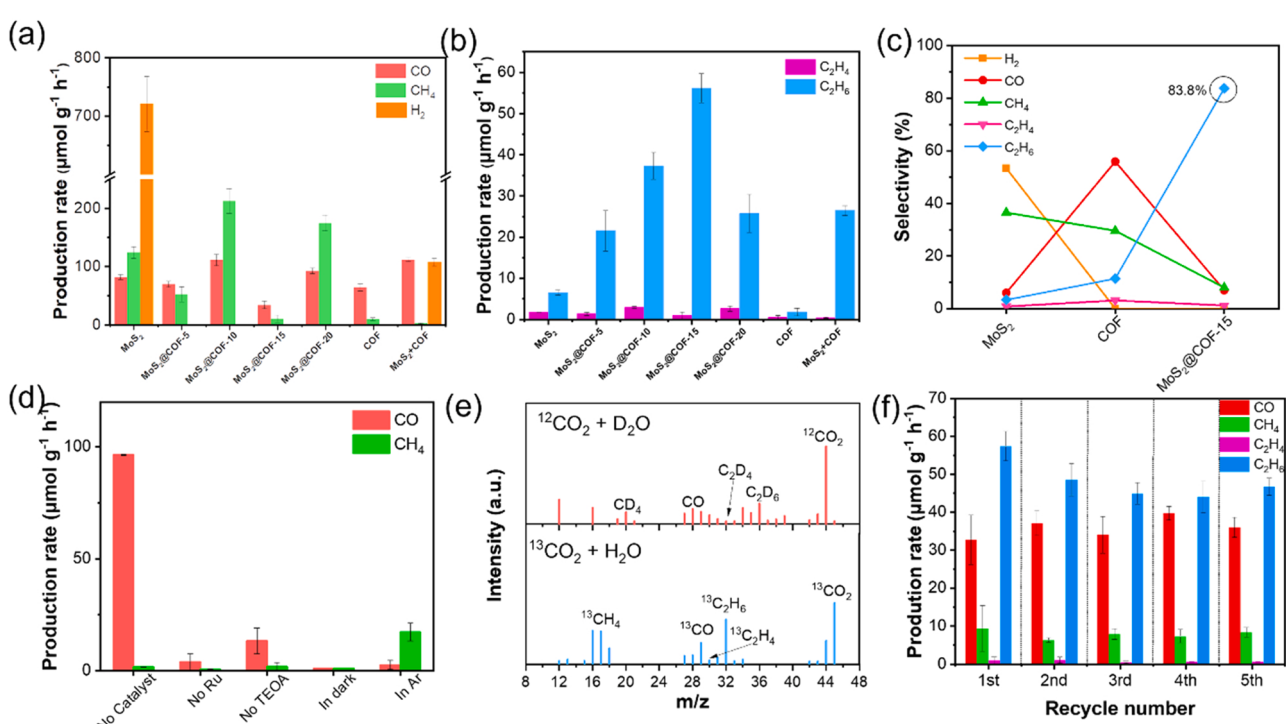


**Fig. 6.** Photocatalytic  $\text{CO}_2$  reduction to (a)  $\text{C}_1$  products and (b)  $\text{C}_2$  products over as-synthesized photocatalysts. (c) Products selectivity of  $\text{CO}_2$  reduction over  $\text{MoS}_2$ , COF, and  $\text{MoS}_2@\text{COF-15}$ . (d) Control experiments over  $\text{MoS}_2@\text{COF-15}$ . (e) GC-MS analysis for photocatalytic  $^{13}\text{CO}_2$  reduction and  $\text{D}_2\text{O}$  over  $\text{MoS}_2@\text{COF-15}$ . (f) Formation rates of  $\text{CO}_2$  products in the stability tests of  $\text{MoS}_2@\text{COF-15}$ .

origins of  $\text{CO}_2$  reduction products. As shown in Fig. 6e, the corresponding  $^{13}\text{CO}_2$  product peak at the peaks at  $m/z = 17, 29$  and  $32$  in the mass spectra might be definitely assigned to  $^{13}\text{CH}_4$ ,  $^{13}\text{CO}$ , and  $^{13}\text{C}_2\text{H}_6$ , respectively, further excluding the possibility of the adsorbed carbonous pollutants on the photocatalyst. Moreover, corresponding  $\text{CD}_4$ ,  $\text{C}_2\text{D}_4$ , and  $\text{C}_2\text{D}_6$  could be detected when using  $\text{D}_2\text{O}$  instead of  $\text{H}_2\text{O}$ , supporting the proton originating from water. The cycling experiments of  $\text{MoS}_2@\text{COF-15}$  heterojunction catalyst have been conducted and revealed that the formation rates of  $\text{CO}_2$  products almost remained unchanged within five consecutive cycles (Fig. 6f). Moreover, FT-IR spectrum and XRD pattern of reused  $\text{MoS}_2@\text{COF-15}$  exhibited no discernible structural change (Figs. S16 and S17), further implying its great photocatalytic stability.

#### 3.4. Photocatalytic $\text{CO}_2$ reduction mechanism

It is well accepted that  $\text{CO}_2$  adsorption and activation on the surface of the catalyst is crucial for photocatalytic  $\text{CO}_2$  reduction. Thus,  $\text{CO}_2$  adsorption-desorption measurements were performed for  $\text{MoS}_2$ , COF

and  $\text{MoS}_2@\text{COF-15}$  composite to assess their  $\text{CO}_2$  adsorption behaviors (Fig. S18). Results indicated that the  $\text{CO}_2$  adsorption capacity of the pure COF reached as high as  $62.7 \text{ cm}^3 \cdot \text{g}^{-1}$  at  $273 \text{ K}$ , whereas  $\text{MoS}_2$  had almost no  $\text{CO}_2$  adsorption capacity in the total pressure due to the lack of porous structure, suggesting that  $\text{CO}_2$  molecule was mainly adsorbed on the surface of COF component. The adsorption capacity of  $\text{MoS}_2@\text{COF-15}$  was slightly lower than that of pristine COF, which is undoubtedly beneficial for subsequent  $\text{CO}_2$  activation and reduction process.

To figure out the activation process of photocatalytic  $\text{CO}_2$  reduction, the in-situ diffuse reflectance infrared Fourier transform spectroscopy (DRIFTS) was performed on  $\text{MoS}_2@\text{COF-15}$  composite along with  $\text{MoS}_2$  and COF for tracking the evolution of reactive species. Two consecutive procedures namely surface adsorption and photocatalysis process were conducted in darkness and under light irradiation, respectively, as shown in Fig. 7a. After pumping  $\text{CO}_2$  and  $\text{H}_2\text{O}$  vapor to saturation in the dark for  $30 \text{ min}$ , multiple intermediates, including bicarbonate ( $\text{HCO}_3^-$ ,  $1419 \text{ cm}^{-1}$ ) [8], monodentate carbonate ( $\text{m-}\text{CO}_3^{2-}$ ,  $1555 \text{ cm}^{-1}$ ), bidentate carbonate ( $\text{b-}\text{CO}_3^{2-}$ ,  $1294 \text{ cm}^{-1}$ ,  $1508 \text{ cm}^{-1}$ ) [60], and active  $\cdot\text{CO}_2$  intermediates ( $1686 \text{ cm}^{-1}$ ) [61] were identified on the  $\text{MoS}_2 @\text{COF-15}$ ,

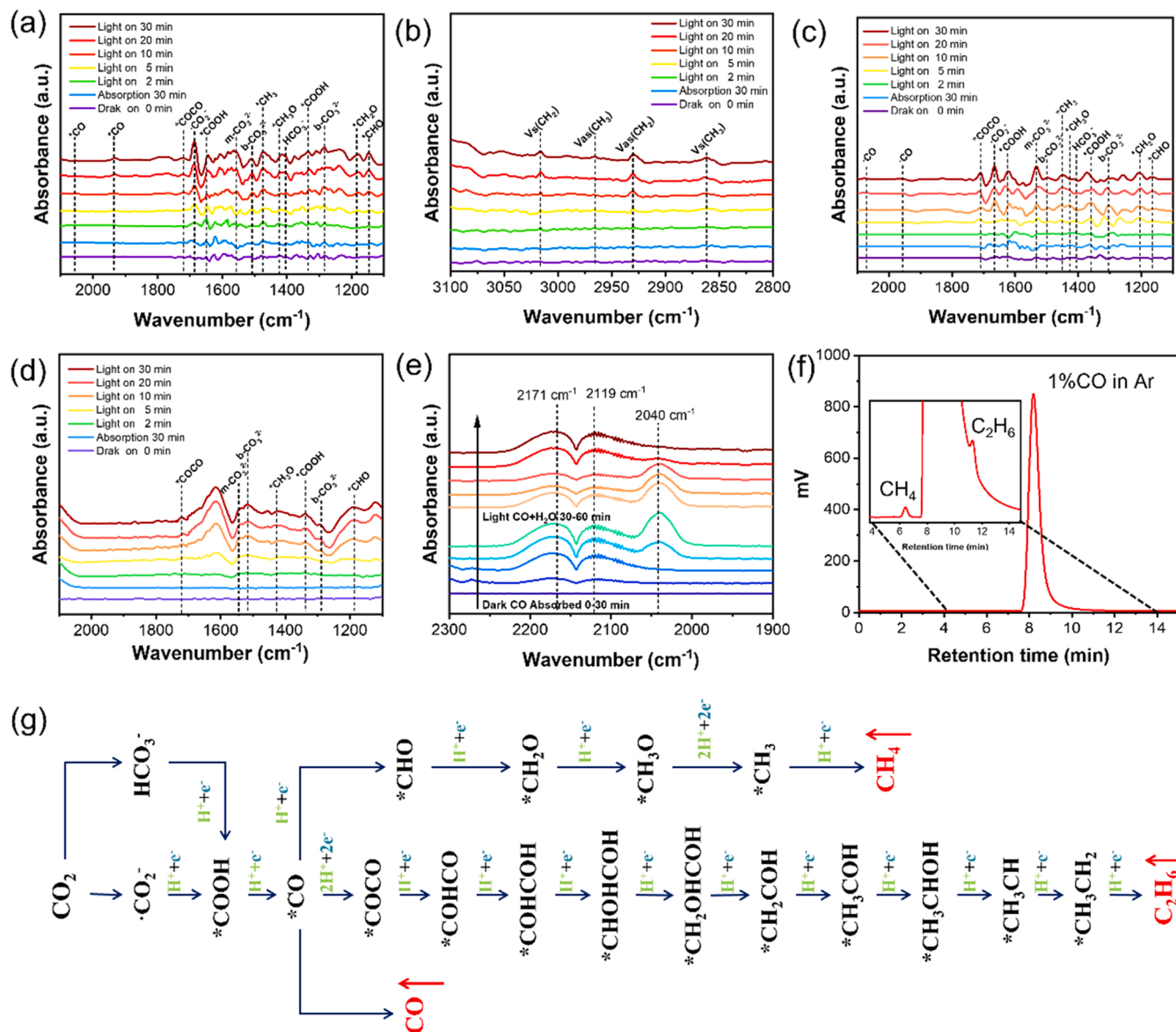


Fig. 7. The in-situ DRIFTS taken during photocatalytic  $\text{CO}_2$  reduction of (a, b)  $\text{MoS}_2@\text{COF-15}$ , (c) COF, and (d)  $\text{MoS}_2$ . (e) The in-situ CO-DRIFTS of  $\text{MoS}_2@\text{COF-15}$ . (f) GC spectra of photocatalytic CO reduction ( $1\% \text{CO}$  in  $\text{Ar}$  gas mixture) over  $\text{MoS}_2@\text{COF-15}$  photocatalyst. (g) Possible reaction pathways for photocatalytic  $\text{CO}_2$  reduction. The “\*” represents adsorption on the substrate.

suggesting the distinct intermediate bonding interaction of adsorbed  $\text{CO}_2$  molecule on the catalyst surface. Upon illumination, it could be observed that the intensity of the absorption peaks generally rises, and several new carbon species, such as formic acid  ${}^*\text{COOH}$  ( $1338 \text{ cm}^{-1}$ ,  $1638 \text{ cm}^{-1}$ ),  ${}^*\text{CHO}$  ( $1147 \text{ cm}^{-1}$ ),  ${}^*\text{CH}_2\text{O}$  ( $1197 \text{ cm}^{-1}$ ) and  ${}^*\text{CH}_3\text{O}$  ( $1436 \text{ cm}^{-1}$ )  ${}^*\text{CO}$  ( $1935 \text{ cm}^{-1}$ ,  $2056 \text{ cm}^{-1}$ ), appeared and increased gradually with prolonged adsorption time [11,62,63]. The symmetric stretching vibrations of  ${}^*\text{CH}_2$  ( $3016 \text{ cm}^{-1}$ ,  $2930 \text{ cm}^{-1}$ ) and  ${}^*\text{CH}_3$  ( $2964 \text{ cm}^{-1}$ ,  $2864 \text{ cm}^{-1}$ ) were also observed under continuous irradiation in Fig. 7b [64], which were critical intermediates for yielding  $\text{CH}_4$ . Importantly, the key intermediate of  ${}^*\text{COCO}$  to obtain  $\text{C}_2$  product could be observed at about  $1716 \text{ cm}^{-1}$ , which provided strong experimental evidence for C-C coupling during the photocatalytic  $\text{CO}_2$  reduction. In addition, intermediates  $\text{HCO}_3^-$  ( $1409 \text{ cm}^{-1}$ ),  $\text{m-}\text{CO}_3^{2-}$  ( $1535 \text{ cm}^{-1}$ ),  $\text{b-}\text{CO}_3^{2-}$  ( $1301 \text{ cm}^{-1}$ ,  $1504 \text{ cm}^{-1}$ ),  ${}^*\text{COOH}$  ( $1358 \text{ cm}^{-1}$ ,  $1630 \text{ cm}^{-1}$ ),  ${}^*\text{CH}_3\text{O}$  ( $1429 \text{ cm}^{-1}$ ),  ${}^*\text{CH}_2\text{O}$  ( $1206 \text{ cm}^{-1}$ )  ${}^*\text{CHO}$  ( $1164 \text{ cm}^{-1}$ ), and  ${}^*\text{COCO}$  ( $1710 \text{ cm}^{-1}$ ) could also be observed in the spectra of pure COF (Fig. 7c). In contrast, almost no adsorption occurred on the pure  $\text{MoS}_2$  in the dark; however, under illumination, partial intermediate species generating  $\text{CO}_2$  reduction products were also detected and increased with prolonged adsorption time (Fig. 7d). To exclude the interferences of solvent ( $\text{CH}_3\text{CN}$ ), sacrificial agent (TEOA) and photocatalyst, the control experiments of in-situ DRIFTS measurements have been conducted to further verify the origins of  $\text{CO}_2$  reduction products (Fig. S19). These results implied that the structure of  $\text{MoS}_2@\text{COF-15}$  composite was the key role in controlling photocatalytic  $\text{CO}_2$  reduction in favor of the C-C coupling pathway to the formation  $\text{C}_2\text{H}_6$  product.

Combining with these results, a possible pathway of  $\text{CO}$ ,  $\text{CH}_4$ , and  $\text{C}_2\text{H}_6$  generation was put forward as shown in Fig. 7g. First,  $\text{CO}_2$  molecule was adsorbed and activated into  $\cdot\text{CO}_2$  species, which forms  $\text{HCO}_3^-$ ,  $\text{CO}_3^{2-}$ , and  ${}^*\text{COOH}$  intermediates and were subsequently reduced to  $\text{CO}$  product. Subsequently, it was speculated that the  ${}^*\text{CO}$  could either be reduced to produce  $\text{CH}_4$  or occur dimerization to form  ${}^*\text{COCO}$  which led to the formation of  $\text{C}_2\text{H}_6$  with the assistance of the  $\text{MoS}_2$  active sites and accelerated electron transfer in the interfaces. To clearly clarify the dimerization of two  ${}^*\text{CO}$  to produce following  $\text{C}_2\text{H}_6$ , which was our main aim, the in-situ DRIFTS tests were thus carried out by directly employing  $\text{CO}$  to replace  $\text{CO}_2$  to probe into the adsorption behavior of  $\text{MoS}_2@\text{COF-15}$  towards the  ${}^*\text{CO}$ . The catalyst was firstly subjected to  $\text{CO}$  adsorption to saturation and then allowed to desorb in purging  $\text{H}_2\text{O}$  vapor, which reacted with  ${}^*\text{CO}$  to subsequent hydrogenation. As shown in Fig. 7e, prior to illumination, the peaks at  $2171$  and  $2119 \text{ cm}^{-1}$  could be observed and assigned to free  $\text{CO}$  molecules adsorbed on the surface [65]. The peak at  $2040 \text{ cm}^{-1}$  was attributed to liner  $\text{CO}$  species adsorbed on the  $\text{MoS}_2@\text{COF-15}$  photocatalyst and increased gradually with prolonged time in darkness, indicating stronger chemical interactions with  ${}^*\text{CO}$  in the heterojunction. However, it was difficult to determine where  $\text{CO}$  was adsorbed on either  $\text{MoS}_2$  or COF. Meanwhile, it was noted that when charging  $\text{H}_2\text{O}$  vapor under light illumination, the  $\text{CO}$  species at  $2040 \text{ cm}^{-1}$  were consumed gradually until disappeared, suggesting that the  ${}^*\text{CO}$  was subsequently reduced to form  $\text{CH}_4$  and  $\text{C}_2\text{H}_6$  products. To further verify this conclusion, we performed the  $\text{CO}$  reduction by using the low concentration  $\text{CO}$  (1%  $\text{CO}$  in Ar gas mixtures) instead of  $\text{CO}_2$  in the  $\text{MoS}_2@\text{COF-15}$  photocatalyst under otherwise identical conditions, and as expected,  $\text{CH}_4$  and  $\text{C}_2\text{H}_6$  products still were detected by gas chromatography (Fig. 7f). Moreover, additional in-situ DRIFTS tests were also conducted by purging  $\text{N}_2$  to desorb adsorbed  $\text{CO}$  from the catalyst. As shown in Fig. S20, the peak at  $2040 \text{ cm}^{-1}$  in CO-DRIFTS retained half intensity after  $\text{N}_2$  purging, whereas the free  $\text{CO}$  molecule disappeared, indicating that  $\text{MoS}_2$  had a higher  $\text{CO}$  chemisorbed affinity due to higher electron density while COF mainly presented physical absorption [66]. It was thus proved that the catalyst structure was crucial for controlling the product distribution of  $\text{CO}_2$  reduction.

To further reveal the mechanism of  $\text{CO}_2$ -to- $\text{C}_2\text{H}_6$  conversion, DFT calculations were performed on the COF and  $\text{MoS}_2$  components of  $\text{MoS}_2@\text{COF-15}$ , respectively. The Gibbs free energy profiles of  ${}^*\text{CO}_2$ -to-

${}^*\text{CO}$  reduction,  ${}^*\text{CO}$ -to- ${}^*\text{COCO}$  dimerization, and  ${}^*\text{C}_2\text{H}_6$  formation were depicted in Fig. 8a. The calculation results suggested that the formations of  ${}^*\text{COOH}$  and  ${}^*\text{COCO}$  were the main rate-limiting steps for both components. The COF component had a much lower kinetic energy barrier (0.54 eV) for  ${}^*\text{CO}_2$  hydrogenation to  ${}^*\text{COOH}$  compared to that on  $\text{MoS}_2$  (2.10 eV), proving that the formation of  ${}^*\text{COOH}$  mainly occurred on the COF. The production of the  ${}^*\text{CO}$  intermediate was exothermic, and  ${}^*\text{CO}$  was easier to adsorb on the  $\text{MoS}_2$  component with higher desorption energy. It has been previously demonstrated experimentally and computationally that the generation of  $\text{C}_2+$  products was determined by the energy barriers of generating  ${}^*\text{COCO}$  via C-C coupling of  ${}^*\text{CO}$ . The process of  ${}^*\text{CO}$  dimerization to  ${}^*\text{COCO}$  on  $\text{MoS}_2$  required a much higher energy input (1.53 eV) compared with that on COF (0.19 eV), which indicated that it was easier to generate  ${}^*\text{COCO}$  at COF. Moreover,  ${}^*\text{CO}$  tended to generate of  ${}^*\text{COCO}$  instead of desorbing  ${}^*\text{CO}$  to  $\text{CO}$  gas, revealing that the heterojunction played a decisive role in C-C coupling. Given that the hydrogen evolution reaction is a thermodynamic competitive process of  $\text{CO}_2$  reduction, the Gibbs free energy of  ${}^*\text{H}$  formation was also calculated. The formation of  ${}^*\text{H}$  on COF required a lower energy barrier (0.52 eV) than that on  $\text{MoS}_2$  (1.97 eV), indicating its better suppression (Fig. 8b). These results suggest that the whole process more tends to occur in COF component of  $\text{MoS}_2@\text{COF}$  heterojunction with the assistance of  $\text{MoS}_2$  in thermodynamics.

Furthermore, during photocatalysis, an electron transfer process from  $[\text{Ru}(\text{bpy})_3]\text{Cl}_2$  to catalyst might be involved by their matched energy levels (Fig. S21). To verify this point, the photoluminescence quenching experiments by adding different amounts of  $\text{MoS}_2@\text{COF-15}$  to a  $\text{CH}_3\text{CN}$  aqueous solution of  $[\text{Ru}(\text{bpy})_3]\text{Cl}_2$  and TEOA were conducted (Fig. 8c), and the intensity of emission peak of  $[\text{Ru}(\text{bpy})_3]\text{Cl}_2$  was continuously quenched with an increasing amount of  $\text{MoS}_2@\text{COF-15}$ , indicating that the recombination of photogenerated electron and holes had been substantially suppressed, in other words, the occurrence of electron transfer from the excited  $[\text{Ru}(\text{bpy})_3]\text{Cl}_2$  to  $\text{MoS}_2@\text{COF-15}$ . Moreover, the fitting of time-resolved luminescence decay profile of  $[\text{Ru}(\text{bpy})_3]\text{Cl}_2$  exhibits a long lifetime of 209.4 ns. When 1.0 mg  $\text{MoS}_2@\text{COF-15}$  was introduced, the photoluminescence of  $[\text{Ru}(\text{bpy})_3]\text{Cl}_2$  was immediately quenched and the average lifetime reduced to 82.1 ns (Fig. S22). These results strongly suggested that the integration of  $\text{MoS}_2@\text{COF-15}$  with photosensitizer was beneficial for charge transfer to trigger this photocatalysis. Finally, the possible mechanism for  $\text{CO}_2$  photoreduction over  $\text{MoS}_2@\text{COF-15}$  is proposed and presented in Fig. 8d. Under light illumination, the photosensitizer  $[\text{Ru}(\text{bpy})_3]^{2+}$  is excited to the excited state, which is capable of donating electrons along with transferring to arrive at the surface of  $\text{MoS}_2@\text{COF-15}$  and forms  $[\text{Ru}(\text{bpy})_3]^{3+}$  [67]. The  $[\text{Ru}(\text{bpy})_3]^{3+}$  is then reductively quenched by sacrificial electron donor TEOA to initial state  $[\text{Ru}(\text{bpy})_3]^{2+}$  to complete the entire cycle by providing electron. The electrons in the CB of  $\text{MoS}_2$  migrate to the HOMO of COF and partially combine with the photoexcited holes, then are further excited to the LUMO of COF. As a result, the electrons accumulated in the LUMO of COF with stronger reducibility to reduce  $\text{CO}_2$ , while others participate in the  $\text{H}_2$  evolution reaction. Meanwhile, the generated  $\text{CO}$  is released as free  $\text{CO}_2$  product and partially adsorbed  $\text{CO}$  molecules are further hydrogenated with the electrons accumulated in the LUMO of COF to form  $\text{CH}_4$  or go through the C-C coupling pathway to form  $\text{C}_2\text{H}_6$  with the assistance of reversible redox process of anthraquinone in the COF [68,69]. The anthraquinone-based reversible redox reaction is believed to be favorable to speed up electron migration and promote continuous hydrogenation of  ${}^*\text{CO}$ , thereby significantly enhancing photocatalytic activity and selectivity.

#### 4. Conclusions

In summary, we have constructed the covalently integrated  $\text{MoS}_2@\text{COF}$  hybrid composites via a multistep synthesis route, in which amino-modified  $\text{MoS}_2$  was wrapped by anthraquinone-based COF and

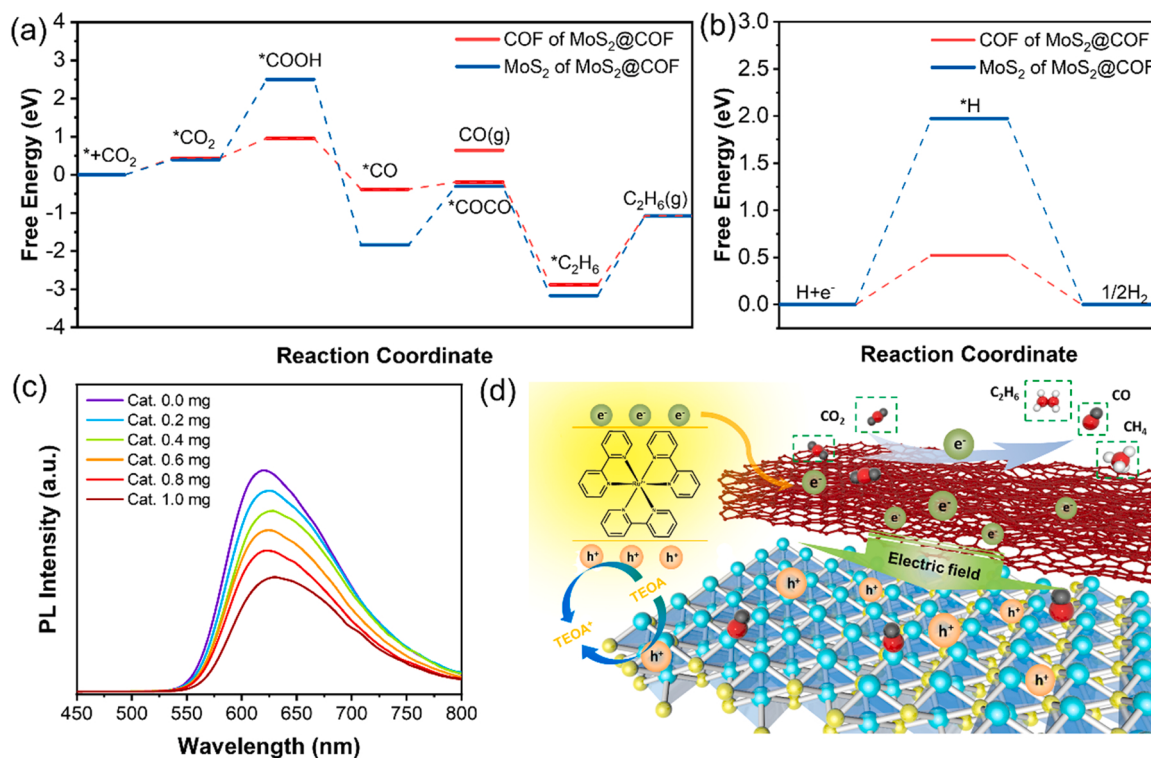


**Fig. 8.** Gibbs free energy profiles of photocatalytic  $\text{CO}_2$  reduction (a) and hydrogen evolution reaction (b) on COF and MoS<sub>2</sub> component of MoS<sub>2</sub>@COF-15. (c) Steady-state fluorescence spectra of  $[\text{Ru}(\text{bpy})_3]\text{Cl}_2$  upon the addition of MoS<sub>2</sub>@COF-15 ( $\lambda_{\text{ex}} = 420 \text{ nm}$ ). (d) Possible mechanism for the  $\text{CO}_2$  reduction by MoS<sub>2</sub>@COF composites.

directed its growth along with amino groups. Experimental observations and DFT calculations demonstrate that the interfacial electric field built in the heterojunction accelerates the photogenerated electrons transfer from MoS<sub>2</sub> to COF under light irradiation, resulting in facilitated charge separation and transfer, and thus effectively promoting the activity and  $\text{C}_2\text{H}_6$  selectivity for photocatalytic  $\text{CO}_2$  reduction. Remarkably, the optimized MoS<sub>2</sub>@COF-15 achieves  $\text{C}_2\text{H}_6$  production rate up to  $56.2 \mu\text{mol}\cdot\text{g}^{-1}\cdot\text{h}^{-1}$  with 83.8% of selectivity, which is 8.6 and 31.2 times higher than that of pure MoS<sub>2</sub> and COF, respectively. The in-situ DRIFTS and DFT calculations indicate that the structure of MoS<sub>2</sub>@COF composite benefits the adsorbed  $\text{CO}_2$  activation and promotes adsorbed CO to convert into  $\text{C}_2\text{H}_6$  product by subsequent hydrogenation and C-C coupling pathway. This work provides new insight into the rational design of photocatalysts for the controllable production of  $\text{C}_2+$  hydrocarbons.

## Supporting information

Supplementary experimental procedures, characterizations including FT-IR spectra and PXRD patterns of pristine MoS<sub>2</sub>, FT-IR spectra, pore size distributions, XPS spectra, Tauc plots, Mott-Schottky plots, experimental estimated band structure diagrams,  $\text{CO}_2$  adsorption-desorption curves, in-situ DRIFTS of as-synthesized MoS<sub>2</sub>, COF and MoS<sub>2</sub>@COF-15, differential charge density map of MoS<sub>2</sub>@COF-15. GC and NMR chromatograms of product sample. FT-IR spectra and XRD patterns of reused and fresh MoS<sub>2</sub>@COF-15.

## Author contributions

The manuscript was written through contributions of all the authors. All authors have given approval to the final version of the manuscript.

## CRediT authorship contribution statement

**Xianheng Yang**: Investigation, Formal analysis, Data curation. **Xingwang Lan**: Methodology, Visualization, Formal analysis, Calculation, Writing – original draft, Project administration. **Yize Zhang**: Investigation. **Hangshuai Li**: Investigation. **Guoyi Bai**: Resources, Supervision, Project administration,

## Declaration of Competing Interest

The authors declare that they have no known competing financial interests or personal relationships that could have appeared to influence the work reported in this paper.

## Data Availability

Data will be made available on request.

## Acknowledgements

This work was supported by the National Natural Science Foundation of China (21908038, 22078080), Science and Technology Project of Hebei Education Department (BJK2022045), Interdisciplinary Research Program of Natural Science of Hebei University (DXK202114). The authors also acknowledge the High-Performance Computing Center of Hebei University.

## Notes

The authors declare no competing financial interest.

## Appendix A. Supporting information

Supplementary data associated with this article can be found in the

online version at doi:10.1016/j.apcatb.2023.122393.

## References

- [1] J. Ran, M. Jaroniec, S.-Z. Qiao, Cocatalysts in semiconductor-based photocatalytic  $\text{CO}_2$  reduction: achievements, challenges, and opportunities, *Adv. Mater.* 30 (2018) 1704649.
- [2] X. Li, J. Yu, M. Jaroniec, X. Chen, Cocatalysts for selective photoreduction of  $\text{CO}_2$  into solar fuels, *Chem. Rev.* 119 (2019) 3962–4179.
- [3] J. Zhao, B. Liu, L. Meng, S. He, R. Yuan, Y. Hou, Z. Ding, H. Lin, Z. Zhang, X. Wang, J. Long, Plasmonic control of solar-driven  $\text{CO}_2$  conversion at the metal/ZnO interfaces, *Appl. Catal. B Environ.* 256 (2019), 117823.
- [4] J. Albero, Y. Peng, H. García, Photocatalytic  $\text{CO}_2$  reduction to  $\text{C}_{2+}$  products, *ACS Catal.* 10 (2020) 5734–5749.
- [5] W. Shao, X. Li, J. Zhu, X. Zu, L. Liang, J. Hu, Y. Pan, J. Zhu, W. Yan, Y. Sun, Y. Xie, Metal<sup>n+</sup>-Metal<sup>n+</sup> pair sites steer C-C coupling for selective  $\text{CO}_2$  photoreduction to  $\text{C}_2$  hydrocarbons, *Nano Res.* 15 (2022) 1882–1891.
- [6] T. Wang, L. Chen, C. Chen, M. Huang, Y. Huang, S. Liu, B. Li, Engineering catalytic interfaces in  $\text{Cu}^{8+}/\text{CeO}_2\text{-TiO}_2$  photocatalysts for synergistically boosting  $\text{CO}_2$  reduction to ethylene, *ACS Nano* 16 (2022) 2306–2318.
- [7] F. Yu, X. Jing, Y. Wang, M. Sun, C. Duan, Hierarchically porous metal-organic framework/MoS<sub>2</sub> interface for selective photocatalytic conversion of  $\text{CO}_2$  with  $\text{H}_2\text{O}$  into  $\text{CH}_3\text{COOH}$ , *Angew. Chem. Int. Ed.* 133 (2021) 25053–25057.
- [8] B. Ni, H. Jiang, W. Guo, Q. Xu, Y. Min, Tailoring the oxidation state of metallic TiO through  $\text{Ti}^{3+}/\text{Ti}^{2+}$  regulation for photocatalytic conversion of  $\text{CO}_2$  to  $\text{C}_2\text{H}_6$ , *Appl. Catal. B Environ.* 307 (2022), 121141.
- [9] Y. Wang, J. Zhao, Y. Liu, G. Liu, S. Ding, Y. Li, J. Xia, H. Li, Synergy between plasmonic and sites on gold nanoparticle-modified bismuth-rich bismuth oxybromide nanotubes for the efficient photocatalytic C-C coupling synthesis of ethane, *J. Colloid Interface Sci.* 616 (2022) 649–658.
- [10] S. Xie, Y. Li, B. Sheng, W. Zhang, W. Wang, C. Chen, J. Li, H. Sheng, J. Zhao, Self-reconstruction of paddle-wheel copper-node to facilitate the photocatalytic  $\text{CO}_2$  reduction to ethane, *Appl. Catal. B Environ.* 310 (2022), 121320.
- [11] N. Li, B. Wang, Y. Si, F. Xue, J. Zhou, Y. Lu, M. Liu, Toward high-value hydrocarbon generation by photocatalytic reduction of  $\text{CO}_2$  in water vapor, *ACS Catal.* 9 (2019) 5590–5602.
- [12] H. Wang, H. Wang, Z. Wang, L. Tang, G. Zeng, P. Xu, M. Chen, T. Xiong, C. Zhou, X. Li, D. Huang, Y. Zhu, Z. Wang, J. Tang, Covalent organic framework photocatalysts: structures and applications, *Chem. Soc. Rev.* 49 (2020) 4135–4165.
- [13] Q. Yang, M. Luo, K. Liu, H. Cao, H. Yan, Covalent organic frameworks for photocatalytic applications, *Appl. Catal. B Environ.* 276 (2020), 119174.
- [14] H.L. Nguyen, A. Alzamly, Covalent organic frameworks as emerging platforms for  $\text{CO}_2$  photoreduction, *ACS Catal.* 11 (2021) 9809–9824.
- [15] S. Lin, C.S. Diercks, Y.B. Zhang, N. Kornienko, E.M. Nichols, Y. Zhao, A.U. Paris, D. Kim, P. Yang, O.M. Yaghi, C.J. Chang, Covalent organic frameworks comprising cobalt porphyrins for catalytic  $\text{CO}_2$  reduction in water, *Science* 349 (2015) 1208–1213.
- [16] X. Wang, Z. Fu, L. Zheng, C. Zhao, X. Wang, S.Y. Chong, F. McBride, R. Raval, M. Bilton, L. Liu, X. Wu, L. Chen, R.S. Sprick, A.I. Cooper, Covalent organic framework nanosheets embedding single cobalt sites for photocatalytic reduction of carbon dioxide, *Chem. Mater.* 32 (2020) 9107–9114.
- [17] Y. Xiang, W. Dong, P. Wang, S. Wang, X. Ding, F. Ichihara, Z. Wang, Y. Wada, S. Jin, Y. Weng, H. Chen, J. Ye, Constructing electron delocalization channels in covalent organic frameworks powering  $\text{CO}_2$  photoreduction in water, *Appl. Catal. B: Environ.* 274 (2020), 119096.
- [18] W. Liu, X. Li, C. Wang, H. Pan, W. Liu, K. Wang, Q. Zeng, R. Wang, J. Jiang, A scalable general synthetic approach toward ultrathin imine-linked two-dimensional covalent organic framework nanosheets for photocatalytic  $\text{CO}_2$  reduction, *J. Am. Chem. Soc.* 141 (2019) 17431–17440.
- [19] S. Barman, A. Singh, F.A. Rahimi, T.K. Maji, Metal-free catalysis: a redox-active donor-acceptor conjugated microporous polymer for selective visible-light-driven  $\text{CO}_2$  reduction to  $\text{CH}_4$ , *J. Am. Chem. Soc.* 143 (2021) 16284–16292.
- [20] S. Yang, W. Hu, X. Zhang, P. He, B. Pattengale, C. Liu, M. Cendejas, I. Hermans, X. Zhang, J. Zhang, J. Huang, 2D covalent organic frameworks as intrinsic photocatalysts for visible light-driven  $\text{CO}_2$  reduction, *J. Am. Chem. Soc.* 140 (2018) 14614–14618.
- [21] W. Zhong, R. Sa, L. Li, Y. He, L. Li, J. Bi, Z. Zhuang, Y. Yu, Z. Zou, Covalent organic framework bearing single Ni sites as a synergistic photocatalyst for selective photoreduction of  $\text{CO}_2$  to  $\text{CO}$ , *J. Am. Chem. Soc.* 141 (2019) 7615–7621.
- [22] Z. Fu, X. Wang, A.M. Gardner, X. Wang, S.Y. Chong, G. Neri, A.J. Cowan, L. Liu, X. Li, A. Vogel, R. Clowes, M. Bilton, L. Chen, R.S. Sprick, A.I. Cooper, A stable covalent organic framework for photocatalytic carbon dioxide reduction, *Chem. Sci.* 11 (2020) 543–550.
- [23] M.-Y. Gao, C.-C. Li, H.-L. Tang, X.-J. Sun, H. Dong, F.-M. Zhang, Boosting visible-light-driven hydrogen evolution of covalent organic frameworks through compositing with MoS<sub>2</sub>: a promising candidate for noble-metal-free photocatalysts, *J. Mater. Chem. A* 7 (2019) 20193–20200.
- [24] W. Liu, J.-H. Wang, J.-Z. Wei, F.-M. Zhang, L.-L. Bai, X.-J. Sun, Boosting visible-light hydrogen evolution of covalent-organic frameworks by introducing Ni-based noble metal-free co-catalyst, *Chem. Eng. J.* 379 (2020), 122342.
- [25] H. Wang, C. Qian, J. Liu, Y. Zeng, D. Wang, W. Zhou, L. Gu, H. Wu, G. Liu, Y. Zhao, Integrating suitable linkage of covalent organic frameworks into covalently bridged inorganic/organic hybrids toward efficient photocatalysis, *J. Am. Chem. Soc.* 142 (2020) 4862–4871.
- [26] C. Cheng, B. He, J. Fan, B. Cheng, S. Cao, J. Yu, An inorganic/organic s-scheme heterojunction  $\text{H}_2$ -production photocatalyst and its charge transfer mechanism, *Adv. Mater.* 33 (2021), 2100317.
- [27] D. Wang, H. Zeng, X. Xiong, M.-F. Wu, M. Xia, M. Xie, J.-P. Zou, S.-L. Luo, Highly efficient charge transfer in CdS-covalent organic framework nanocomposites for stable photocatalytic hydrogen evolution under visible light, *Sci. Bull.* 65 (2020) 113–122.
- [28] Y. Wang, Z. Hu, W. Wang, H. He, L. Deng, Y. Zhang, J. Huang, N. Zhao, G. Yu, Y.-N. Liu, Design of well-defined shell–core covalent organic frameworks/metal sulfide as an efficient Z-scheme heterojunction for photocatalytic water splitting, *Chem. Sci.* 12 (2021) 16065–16073.
- [29] N. He, X. Zhu, F. Liu, R. Yu, Z. Xue, X. Liu, Rational design of FeS<sub>2</sub>-encapsulated covalent organic frameworks as stable and reusable nanozyme for dual-signal detection glutathione in cell lysates, *Chem. Eng. J.* 445 (2022), 136543.
- [30] L. Wang, G. Huang, L. Zhang, R. Lian, J. Huang, H. She, C. Liu, Q. Wang, Construction of  $\text{TiO}_2$ -covalent organic framework Z-Scheme hybrid through coordination bond for photocatalytic  $\text{CO}_2$  conversion, *J. Energy Chem.* 64 (2022) 85–92.
- [31] M. Zhang, M. Lu, Z.-L. Lang, J. Liu, M. Liu, J.-N. Chang, L.-Y. Li, L.-J. Shang, M. Wang, S.-L. Li, Y.-Q. Lan, Semiconductor/covalent-organic-framework Z-scheme heterojunctions for artificial photosynthesis, *Angew. Chem. Int. Ed.* 132 (2020) 6562–6568.
- [32] X. An, J. Bian, K. Zhu, R. Liu, H. Liu, J. Qu, Facet-dependent activity of  $\text{TiO}_2$ /covalent organic framework S-scheme heterostructures for  $\text{CO}_2$  photoreduction, *Chem. Eng. J.* 442 (2022), 135279.
- [33] Y. Peng, M. Zhao, B. Chen, Z. Zhang, Y. Huang, F. Dai, Z. Lai, X. Cui, C. Tan, H. Zhang, Hybridization of MOFs and COFs: a new strategy for construction of MOF@COF core-shell hybrid materials, *Adv. Mater.* 30 (2018), 1705454.
- [34] F.-M. Zhang, J.-L. Sheng, Z.-D. Yang, X.-J. Sun, H.-L. Tang, M. Lu, H. Dong, F.-C. Shen, J. Liu, Y.-Q. Lan, Rational design of MOF/COF hybrid materials for photocatalytic  $\text{H}_2$  evolution in the presence of sacrificial electron donors, *Angew. Chem. Int. Ed.* 57 (2018) 12106–12110.
- [35] P. Xue, X. Pan, J. Huang, Y. Gao, W. Guo, J. Li, M. Tang, Z. Wang, In situ fabrication of porous MOF/COF hybrid photocatalysts for visible-light-driven hydrogen evolution, *ACS Appl. Mater. Interfaces* 13 (2021) 59915–59924.
- [36] C.-X. Chen, Y.-Y. Xiong, X. Zhong, P.C. Lan, Z.-W. Wei, H. Pan, P.-Y. Su, Y. Song, Y.-F. Chen, A. Nafady, S. Sirajuddin, E. Ma, Enhancing photocatalytic hydrogen production via the construction of robust multivariate Ti-MOF/COF, *Compos., Angew. Chem. Int. Ed.* 61 (2022) e202114071.
- [37] J. Wang, Y. Yu, J. Cui, X. Li, Y. Zhang, C. Wang, X. Yu, J. Ye, Defective g-C<sub>3</sub>N<sub>4</sub>/covalent organic framework van der Waals heterojunction toward highly efficient S-scheme  $\text{CO}_2$  photoreduction, *Appl. Catal. B Environ.* 301 (2022), 120814.
- [38] Y. Xing, L. Yin, Y. Zhao, Z. Du, H.-Q. Tan, X. Qin, W. Ho, T. Qiu, Y.-G. Li, Construction of the 1D covalent organic framework/2D g-C<sub>3</sub>N<sub>4</sub> heterojunction with high apparent quantum efficiency at 500 nm, *ACS Appl. Mater. Interfaces* 12 (2020) 51555–51562.
- [39] Y. Hou, C.-X. Cui, E. Zhang, J.-C. Wang, Y. Li, Y. Zhang, Y. Zhang, Q. Wang, J. Jiang, A hybrid of g-C<sub>3</sub>N<sub>4</sub> and porphyrin-based covalent organic frameworks via liquid-assisted grinding for enhanced visible-light-driven photoactivity, *Dalton Trans.* 48 (2019) 14989–14995.
- [40] Y. Zou, B. Yang, Y. Liu, Y. Ren, J. Ma, X. Zhou, X. Cheng, Y. Deng, Controllable interface-induced Co-assembly toward highly ordered mesoporous Pt@ $\text{TiO}_2$ /g-C<sub>3</sub>N<sub>4</sub> heterojunctions with enhanced photocatalytic performance, *Adv. Funct. Mater.* 28 (2018), 1806214.
- [41] J. Yang, J. Jing, W. Li, Y. Zhu, Electron donor–acceptor interface of TPPS/PDI boosting charge transfer for efficient photocatalytic hydrogen evolution, *Adv. Sci.* 9 (2022), 2201134.
- [42] R. Gusalin, N. Kumar, F. Opoku, P.P. Govender, S.S. Ray, MoS<sub>2</sub> nanosheet/ZnS composites for the visible-light-assisted photocatalytic degradation of oxytetracycline, *ACS Appl. Nano Mater.* 4 (2021) 4721–4734.
- [43] Y. Liu, X. Xu, J. Zhang, H. Zhang, W. Tian, X. Li, M.O. Tade, H. Sun, S. Wang, Flower-like MoS<sub>2</sub> on graphitic carbon nitride for enhanced photocatalytic and electrochemical hydrogen evolutions, *Appl. Catal. B Environ.* 239 (2018) 334–344.
- [44] W. Zhou, Z. Yin, Y. Du, X. Huang, Z. Zeng, Z. Fan, H. Liu, J. Wang, H. Zhang, Synthesis of few-layer MoS<sub>2</sub> nanosheet-coated  $\text{TiO}_2$  nanobelt heterostructures for enhanced photocatalytic actives, *Small* 9 (2013) 140–147.
- [45] W. Guan, Y. Li, Q. Zhong, H. Liu, J. Chen, H. Hu, K. Lv, J. Gong, Y. Xu, Z. Kang, M. Cao, Q. Zhang, Fabricating MAPbI<sub>3</sub>/MoS<sub>2</sub> composites for improved photocatalytic performance, *Nano Lett.* 21 (2021) 597–604.
- [46] C.R. DeBlase, K.E. Silberstein, T.-T. Truong, H.D. Abruna, W.R. Dichtel,  $\beta$ -Ketoenamine-linked covalent organic frameworks capable of pseudocapacitive energy storage, *J. Am. Chem. Soc.* 135 (2013) 16821–16824.
- [47] P. Xia, S. Cao, B. Zhu, M. Liu, M. Shi, J. Yu, Y. Zhang, Designing a 0D/2D S-scheme heterojunction over polymeric carbon nitride for visible-light photocatalytic inactivation of bacteria, *Angew. Chem. Int. Ed.* 59 (2020) 5218–5225.
- [48] N. Li, X. Chen, J. Wang, X. Liang, L. Ma, X. Jing, D.-L. Chen, Z. Li, ZnSe nanorods-CsSnCl<sub>3</sub> perovskite heterojunction composite for photocatalytic  $\text{CO}_2$  reduction, *ACS Nano* 16 (2022) 3332–3340.
- [49] X. Zhang, F. Tian, X. Lan, Y. Liu, W. Yang, J. Zhang, Y. Yu, Building P-doped MoS<sub>2</sub>/g-C<sub>3</sub>N<sub>4</sub> layered heterojunction with a dual-internal electric field for efficient photocatalytic sterilization, *Chem. Eng. J.* 429 (2022), 132588.
- [50] F. Liu, R. Shi, Z. Wang, Y. Weng, C.M. Che, Y. Chen, Direct Z-scheme hetero-phase junction of black/red phosphorus for photocatalytic water splitting, *Angew. Chem. Int. Ed.* 58 (2019) 11791–11795.
- [51] Y. Qin, H. Li, J. Lu, Y. Feng, F. Meng, C. Ma, Y. Yan, M. Meng, Synergy between van der waals heterojunction and vacancy in ZnIn<sub>2</sub>S<sub>4</sub>/g-C<sub>3</sub>N<sub>4</sub> 2D/2D photocatalysts for

- enhanced photocatalytic hydrogen evolution, *Appl. Catal. B Environ.* 277 (2020), 119254.
- [52] X. Chen, J. Wang, Y. Chai, Z. Zhang, Y. Zhu, Efficient photocatalytic overall water splitting induced by the giant internal electric field of a g-C<sub>3</sub>N<sub>4</sub>/rGO/PPDIP Z-scheme heterojunction, *Adv. Mater.* 33 (2021), 2007479.
- [53] Z.Y. Guo, C.X. Li, M. Gao, X. Han, Y.J. Zhang, W.J. Zhang, W.W. Li, Mn-O covalency governs the intrinsic activity of Co-Mn spinel oxides for boosted peroxymonosulfate activation, *Angew. Chem. Int. Ed.* 60 (2021) 274–280.
- [54] P. Chen, B. Lei, X. Dong, H. Wang, J. Sheng, W. Cui, J. Li, Y. Sun, Z. Wang, F. Dong, Rare-earth single-atom La-N charge-transfer bridge on carbon nitride for highly efficient and selective photocatalytic CO<sub>2</sub> reduction, *ACS Nano* 14 (2020) 15841–15852.
- [55] L. Cheng, H. Yin, C. Cai, J. Fan, Q. Xiang, Single Ni atoms anchored on porous few-layer g-C<sub>3</sub>N<sub>4</sub> for photocatalytic CO<sub>2</sub> reduction: the role of edge confinement, *Small* 16 (2020), 2002411.
- [56] Z. Mu, S. Chen, Y. Wang, Z. Zhang, Z. Li, B. Xin, L. Jing, Controlled construction of copper phthalocyanine/α-Fe<sub>2</sub>O<sub>3</sub> ultrathin S-scheme heterojunctions for efficient photocatalytic CO<sub>2</sub> reduction under wide visible-light irradiation, *Small Sci.* 1 (2021), 2100050.
- [57] Y. Xi, X. Zhang, Y. Shen, W. Dong, Z. Fan, K. Wang, S. Zhong, S. Bai, Aspect ratio-dependent photocatalytic enhancement of CsPbBr<sub>3</sub> in CO<sub>2</sub> reduction with two-dimensional metal organic framework as a cocatalyst, *Appl. Catal. B Environ.* 297 (2021), 120411.
- [58] Y. Liang, X. Wu, X. Liu, C. Li, S. Liu, Recovering solar fuels from photocatalytic CO<sub>2</sub> reduction over W<sup>6+</sup>-incorporated crystalline g-C<sub>3</sub>N<sub>4</sub> nanorods by synergistic modulation of active centers, *Appl. Catal. B Environ.* 304 (2022), 120978.
- [59] Y. Zhang, D. Yao, B. Xia, M. Jaroniec, J. Ran, S.-Z. Qiao, Photocatalytic CO<sub>2</sub> reduction: identification and elimination of false-positive results, *ACS Energy Lett.* 7 (2022) 1611–1617.
- [60] X. Yu, V. De Waele, A. Löfberg, Selective photocatalytic conversion of methane into carbon monoxide over zinc-heteropolyacid-titania nanocomposites, *Nat. Commun.* 10 (2019) 700.
- [61] L. Cheng, X. Yue, L. Wang, D. Zhang, P. Zhang, J. Fan, Q. Xiang, Dual-single-atom tailoring with bifunctional integration for high-performance CO<sub>2</sub> photoreduction, *Adv. Mater.* 33 (2021), 2105135.
- [62] J. Fan, Y. Zhao, H. Du, L. Zheng, M. Gao, D. Li, J. Feng, Light-induced structural dynamic evolution of Pt single atoms for highly efficient photocatalytic CO<sub>2</sub> reduction, *ACS Appl. Mater. Interfaces* 14 (2022) 26752–26765.
- [63] W. Wang, C. Deng, S. Xie, Y. Li, W. Zhang, H. Sheng, C. Chen, J. Zhao, Photocatalytic C-C coupling from carbon dioxide reduction on copper oxide with mixed-valence copper(I)/Copper(II), *J. Am. Chem. Soc.* 143 (2021) 2984–2993.
- [64] R.H. Zhang, H. Wang, S.Y. Tang, C.J. Liu, F. Dong, H.R. Yue, B. Liang, The photocatalytic oxidative dehydrogenation of ethane using CO<sub>2</sub> as a soft oxidant over Pd/TiO<sub>2</sub> catalysts to C<sub>2</sub>H<sub>4</sub> and syngas, *ACS Catal.* 8 (2018) 9280–9286.
- [65] P. Liu, Z. Huang, X. Gao, X. Hong, J. Zhu, G. Wang, Y. Wu, J. Zeng, X. Zheng, Synergy between palladium single atoms and nanoparticles via hydrogen spillover for enhancing CO<sub>2</sub> photoreduction to CH<sub>4</sub>, *Adv. Mater.* 34 (2022), 2200057.
- [66] A.A. Zhang, D. Si, H. Huang, L. Xie, Z.-B. Fang, T.-F. Liu, R. Cao, Partial metalation of porphyrin moieties in hydrogen-bonded organic frameworks provides enhanced CO<sub>2</sub> photoreduction activity, *Angew. Chem. Int. Ed.* 134 (2022) e202203955.
- [67] X. Yao, K. Chen, L.-Q. Qiu, Z.-W. Yang, L.-N. He, Ferric porphyrin-based porous organic polymers for CO<sub>2</sub> photocatalytic reduction to syngas with selectivity control, *Chem. Mater.* 33 (2021) 8863–8872.
- [68] Z. Wang, L. Zeng, C. He, C. Duan, Metal-organic framework-encapsulated anthraquinone for efficient photocatalytic hydrogen atom transfer, *ACS Appl. Mater. Interfaces* 14 (2022) 7980–7989.
- [69] F. Yu, Z. Zhu, C. Li, W. Li, R. Liang, S. Yu, Z. Xu, F. Song, Q. Ren, Z. Zhang, Redox-active perylene-anthraquinone donor-acceptor conjugated microporous polymer with an unusual electron delocalization channel for photocatalytic reduction of uranium (VI) in strongly acidic solution, *Appl. Catal. B Environ.* 314 (2022), 121467.